



#### **OPEN ACCESS**

EDITED BY Jinxu Mo, Dongguan University of Technology, China

REVIEWED BY Songzhao Qu, Henan University of Urban Construction, China Supasit Srivaranun. Kasetsart University, Thailand Rui Zhang, ETH Zurich, Switzerland

\*CORRESPONDENCE

Sandra Villamizar.

Ghadir Haikal,

□ ghaikal@ncsu.edu

RECEIVED 31 August 2025 REVISED 07 October 2025 ACCEPTED 09 October 2025 PUBLISHED 11 November 2025

#### CITATION

Villamizar S, Abdelaleim O, Gomez D, Ramirez J and Haikal G (2025) Performance assessment of deck link slabs in multi-span bridges: a case study of the Plott Creek Bridge.

Front. Built Environ. 11:1696051. doi: 10.3389/fbuil.2025.1696051

© 2025 Villamizar, Abdelaleim, Gomez, Ramirez and Haikal. This is an open-access article distributed under the terms of the Creative Commons Attribution License (CC BY). The use, distribution or reproduction in other forums is permitted, provided the original author(s) and the copyright owner(s) are credited and that the original publication in this journal is cited, in accordance with accepted academic practice. No use, distribution or reproduction is permitted which does not comply with these terms.

# Performance assessment of deck link slabs in multi-span bridges: a case study of the Plott Creek Bridge

Sandra Villamizar<sup>1,2</sup>\*, Osama Abdelaleim<sup>2</sup>, Daniel Gomez<sup>3</sup>, Julio Ramirez<sup>2</sup> and Ghadir Haikal<sup>4</sup>\*

<sup>1</sup>College of Engineering, Universidad Santiago de Cali, Cali, Colombia, <sup>2</sup>Lyles School of Civil and Construction Engineering, Purdue University, West Lafayette, IN, United States, <sup>3</sup>School of Civil Engineering and Geomatics, Universidad del Valle, Cali, Colombia, <sup>4</sup>Department of Civil, Construction and Environmental Engineering, North Carolina State University, Raleigh, NC, United States

The use of link-slab connections in simply supported multi-span bridge decks is a widely adopted strategy to minimize the number of expansion joints, reducing long-term maintenance issues and improving the roadway surface quality. Current design practice for debonded link slabs primarily focuses on live loads, assuming that the girders behave as simple spans while neglecting the influence of girder support conditions. The link slab is typically considered to be in pure bending and is designed to accommodate girder end rotation. A bond-breaker material is employed between the top of the girders and the bottom of the link slab to reduce the induced stresses and control cracking at the connection region. Within the debonded length, typically set at 5% of each span length, the existing stirrups and shear connectors are removed. Additionally, adequate reinforcement is provided to satisfy crack width control requirements at service limit states. Despite these measures, field observations indicate persistent cracking and leakage issues in link slabs early in their service life. Several investigations suggest that temperature gradients and shrinkage effects are primary contributors to these cracks. Additionally, studies have shown that link slabs experience both axial tension and bending, challenging the assumption of pure bending behavior. The novelty of this study lies in quantifying the effects of thermal gradients within the widely used simplified design framework, thereby providing engineers with practical metrics to adapt the method for improved design accuracy. A numerical evaluation of the response of link slabs is performed using finite element analysis to model the combined effects of traffic loads and vertical temperature gradients. The slabs are analyzed under HL-93 loading and temperature gradients following AASHTO LRFD Bridge Design Specifications. A parametric study is conducted to examine the influence of girder support conditions and debonded length on link slab performance. The computational results highlight the significant role of temperature gradients and girder support conditions in inducing elevated stresses and promoting crack formation at the link slab. The findings presented in this paper emphasize the need to account for these parameters in the design of link slabs to enhance their durability and structural performance. Moreover, the applicability of the simplified rotation-based design approach is reaffirmed, with proposed

modifications enabling it to capture the combined effects of live load and thermal gradients.

KEYWORDS

link slab, jointless deck, bridge rehabilitation, serviceability, debonding, temperature effects

# 1 Introduction

Bridge deck joints, typically located at the ends of spans over piers and at abutments, are designed to accommodate superstructure movements caused by shrinkage, creep, live loads, and thermal effects. However, expansion joints have long been associated with durability problems, including water and debris infiltration, which accelerate deterioration of substructure elements and increase maintenance costs. As a result, transportation agencies across the United States have tried for decades to minimize or eliminate these joints. A link slab is a cast-in-place concrete element that provides continuity to the deck slab, while the supporting girders remain simply supported between adjacent spans. By eliminating the expansion joint, link slabs help reduce maintenance and repair costs associated with joint leakage and improve the overall quality of the bridge riding surface. The concept has been proposed for use with steel and concrete beam bridge superstructure (Gastal, 1986).

Two primary configurations of link slabs are: bonded and debonded. In bonded link slabs, the concrete is cast directly over the girders, enabling composite action between the deck and the supporting beams. In contrast, debonded link slabs incorporate bond breakers and do not include shear connectors in the joint region to prevent composite interaction between the deck and girders (Caner and Zia, 1998; Culmo et al., 2017). Debonded link slabs can be constructed as either full-depth or partial-depth, where the depth refers to the total thickness of the bridge deck. A full-depth link slab has the same thickness as the deck. These slabs may be built using either precast or cast-in-place concrete (Gergess, 2019; Gergess and Hawi, 2019).

Current design practices for debonded link slabs in the United States and Canada are largely based on the methodology proposed by Caner and Zia (1998). This method models the link slab as a pure bending element that resists moments generated by girder end rotations under live load plus impact, assuming simple-span girders and neglecting continuity across the joint. The slab stiffness is considered low relative to the girder, and load transfer mechanisms such as shear studs and stirrups are removed in the debonded zone, typically defined as 5% of the span length on each side of the joint, as shown in Figure 1. A bond-breaker is introduced between the girder tops and the slab bottom to reduce stresses.

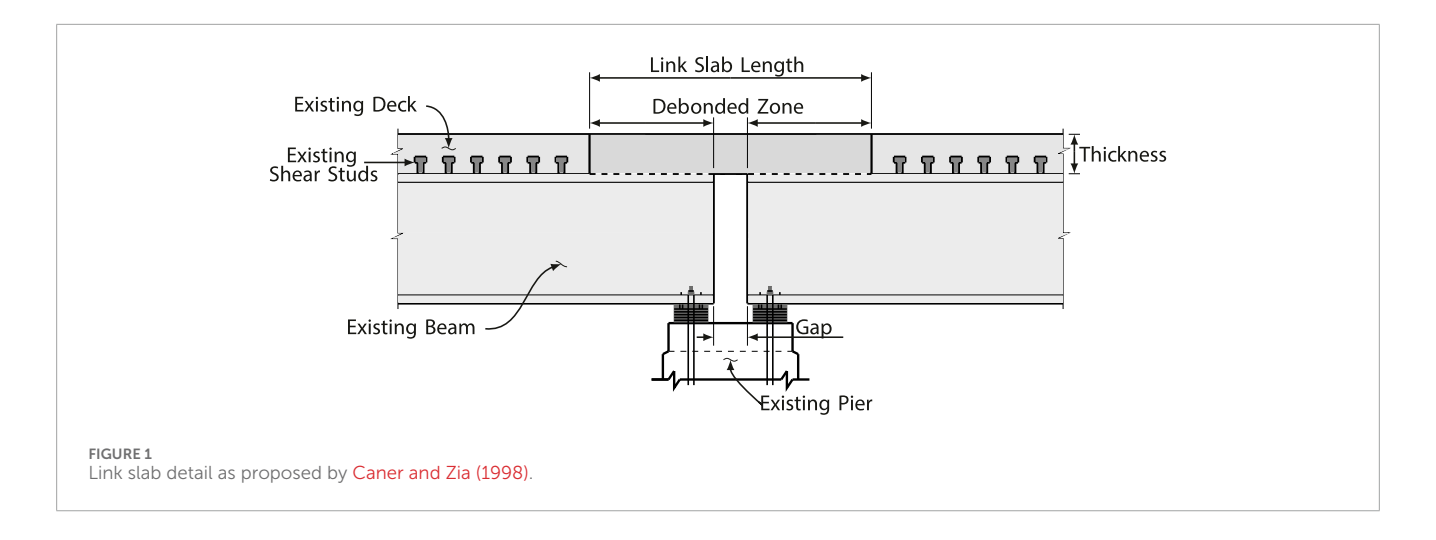
The moment applied at the ends of the link slab  $(M_a)$  is determined using Equation 1, expressed as

$$M_a = \frac{2E_c I_{ls}}{L_{ls}} \theta_g \tag{1}$$

where,  $E_c$  = elasticity modulus of the link-slab concrete;  $I_{ls}$  = moment of inertia of the link slab based on the gross section properties;  $L_{ls}$  = total length of the link slab;  $\theta_g$  = maximum end rotations of the girders as simply-supported.

Although the simplified approach proposed by Caner and Zia (1998) has been widely adopted in practice, it overlooks key variables that can significantly influence link slab performance, including girder support conditions and thermal gradients which are the focus of this paper. Moreover, the influence of the debonded length remains insufficiently understood. Early 2D finite element studies (Gastal, 1986; Gastal and Zia, 1989; ElSafty, 1994; Caner, 1996; Caner et al., 2002; ElSafty and Okeil, 2008) indicated that the link slab could experience either full tension or full compression depending on the girder support type. However, more recent 3D numerical studies (Aktan et al., 2008; Ulku et al., 2009; Luo et al., 2024) have challenged this assumption, showing that link slabs are subjected to a combination of axial tension and bending, thereby emphasizing the need to incorporate realistic boundary conditions in the design process. Au et al. (2013) observed unrealistic deformation patterns when conducting three-dimensional analyses and introduced an adjustment factor in Equation 1, based on the distance between adjacent simple supports at the pier location, to better capture the displacement compatibility between the link slabs and supporting girders.

Temperature gradients represent another critical factor, as they generate internal stresses that, when combined with traffic loads, contribute to cracking. Research studies (Aktan et al., 2008; Haikal et al., 2019) have reported widespread cracking in rehabilitated link slabs, which were designed using the Caner and Zia (1998) method. Observed crack widths were large enough to permit moisture ingress, accelerating the deterioration of underlying structural components (Kim et al., 2004; Hong, 2014; Leivamaldonado et al., 2023). These findings have raised concerns about the suitability of current design methodologies. Ulku et al. (2009) used non-linear finite element modeling to evaluate the behavior of link slabs on concrete bridges. Their study incorporated temperature gradients and girder end-rotation effects by applying curvature and strain compatibility principles to compute thermally induced forces. The results showed that negative temperature gradients significantly increase tensile stresses in the top fiber of the slab, particularly under certain support configurations. The authors recommended using moment-axial force interaction diagrams to improve crack control. However, their proposed design recommendations are not yet in standard use and were based on a specific Michigan detail with discontinuous bottom reinforcement. Similarly, Gergess (2019) estimated the negative moment in the link slabs by analyzing the difference in curvature between the girders and the slab in the debonded zone, using the exact deformed shape under live load. Their analysis assumed elastic behavior and did not account for girder support conditions or thermal loads. Luo et al. (2024) proposed a refined analytical method that introduces the concept of a girder end rotation reduction coefficient to better account for the interaction of the link slab with adjacent spans. Their method



achieved improved accuracy in predicting internal forces through model and site validation.

To address durability concerns, recent studies have explored advanced concrete materials that improve crack control and accelerate construction. High-performance and fiber-reinforced concretes, such as Engineered Cementitious Composite (ECC), Latex Modified Concrete (LMC), Ultra High Ductility Cementitious Composites (UHDCC), and Ultra High Performance Concrete (UHPC), are being promoted by transportation agencies in Virginia, Michigan, and New York (Lepech and Li, 2008; 2009; Ozyildirim et al., 2017; Zheng et al., 2018; Hou et al., 2018; Zhong et al., 2019; Garber et al., 2023; Li et al., 2005; Zhang et al., 2002; Qian et al., 2009). These materials offer benefits including reduced shrinkage, enhanced bond properties, and high early strength, which are vital to minimizing cracking and joint leakage (Li et al., 2003; Li et al., 2008; Fu and Zhu, 2017). In parallel, alternative reinforcement options such as Fiber Reinforced Polymer (FRP) bars have been investigated as a corrosion-resistant alternative to traditional steel reinforcement (Reyes and Robertson, 2011; Larusson et al., 2013; Saber and Aleti, 2012; Shafei et al., 2018; Karim and Shafei, 2021). Although material innovations are being explored to improve crack control and durability, limited research has addressed improvements in link slab design. A comprehensive understanding of how structural parameters influence link slab behavior remains essential. Parameters such as girder support configuration and debonded zone size require further investigation to ensure reliable performance, particularly under the combined effects of mechanical and thermal loading.

The objective of this study is to assess the applicability of the simplified design framework proposed by Caner and Zia (1998) under combined live load and thermal loading conditions, in accordance with the provisions of the AASHTO LRFD Bridge Design Specifications (AASHTO, 2017). In particular, the research presented here focuses on full-depth, cast-in-place debonded link slab configurations applied to steel and concrete girders for joint replacement. In this context, the dead load effects from the girders and existing deck are assumed to have already taken place prior to the construction of the link slab. Consequently, time-dependent phenomena such as creep, drying/autogenous shrinkage of concrete, and steel relaxation are not considered.

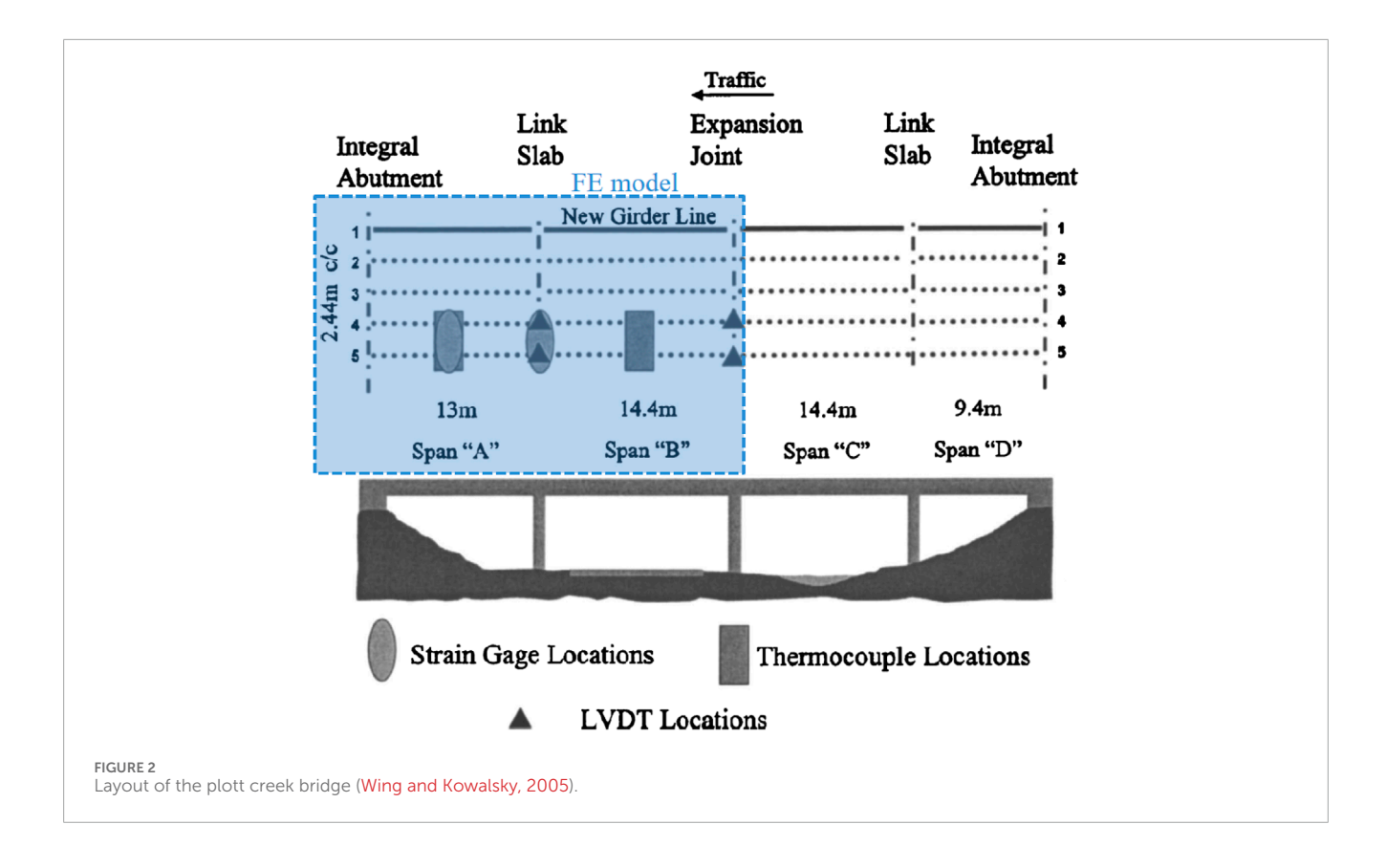
Recent advances in bridge diagnostics highlight the importance of integrating field observations with validated numerical models to link observed damage mechanisms to their underlying structural responses (Srivaranun et al., 2024; Jirawattanasomkul et al., 2021). A central challenge in this process lies in translating discrete field measurements, such as strains, displacements, or crack widths, into a comprehensive understanding of the internal stress states and load-transfer mechanisms driving structural behavior. Field data often capture localized responses influenced by boundary conditions, environmental variations, and measurement limitations, making it difficult to directly infer the governing mechanics. Validated numerical models serve as a critical bridge between measurement and mechanism by enabling the interpretation of observed responses within a consistent analytical framework (Wang et al., 2019; Karim and Shafei, 2021; Luo et al., 2024). This study follows this contemporary methodological approach by employing a validated model of the Plott Creek Bridge in North Carolina, originally monitored by Wing and Kowalsky (2005), to replicate realistic field conditions and examine the effects of support type and debonded length on link slab cracking behavior. The findings offer valuable insight for refining current design and detailing practices, addressing key limitations of existing methods, and advancing the reliability of jointless bridge systems.

Section 1 reviews the background and motivation of the study. Section 2 presents the structural configuration and numerical model for the Plott Creek Bridge. Sections 3 and 4 present the analysis results under service loads and parametric studies, respectively. Section 5 concludes with major findings and recommendations for practice.

# 2 Bridge structure

# 2.1 Description

The Plott Creek Bridge in Haywood country in North Carolina, investigated by Wing and Kowalsky (2005), serves as the reference bridge configuration and geometry for the present study. The authors instrumented two of the four spans to examine the long-term performance of the bridge structure after its deck rehabilitation



with link slabs. The rehabilitated bridge has an overall length of 51.2 m (2016 in.) and is 11.9 m (468 in.) wide. It accommodates three southbound lanes of traffic. The superstructure consists of an 0.20 m (8 in.) reinforced concrete deck slab supported by five steel beams W36 × 150 spaced at 2.44 m (96 in.) center to center. Two of the three-deck connections over the piers are rehabilitated using reinforced concrete link slabs, designed according to the approach proposed by Caner and Zia (1998). The abutments are poured monolithically with the steel beams. The total length of the link slab is 1.70 m (67 in.), which includes 0.05 m (2 in.) gap between adjacent spans. The plan view of the multi-simple-span Plott Creek Bridge is shown in Figure 2. In this study, a numerical model for the Plott Creek Bridge is developed to comprehensively investigate the behavior of the link slab under various loading conditions. The modeling approach and analysis procedures are summarized in the following sections. A complete description of this work is provided in Villamizar (2024).

#### 2.2 Finite element model

#### 2.2.1 Assembly

A three-dimensional finite element (FE) model of the Plott Creek Bridge in Haywood country is developed in ABAQUS Standard (ABAQUS, 2020) to study the effect of traffic loads and temperature gradients on the behavior of link slabs. The FE model represents the two spans (A and B) instrumented by Wing and Kowalsky (2005) resulting in a 27.4 m (1,079 in.) long steel girder bridge, as shown in Figures 2, 3. Each bridge component (i.e., deck slab, supporting girder, link slab, and concrete parapet) is modeled

using eight-node trilinear displacement and temperature elements (C3D8T). The reinforcing bars are modeled using two-node 3D thermally coupled truss elements (T3D2T) and embedded into concrete elements, assuming a perfect bond. All parts, except the girder ends at the joint location (debonded zone) are fully bonded. Tie constraints are created to simulate the full composite action between the concrete deck slab and girders and the bond strength between the deck and link slab interface. As the studied link slabs did not include bond failure, using tie constraints to model the cold joint formed when casting two concretes at different times is a reasonable approach. A tie constraint is also employed to simulate the interface between the parapet and deck slab, considering that both parts are perfectly joined together through steel reinforcing bars. Supports at beam ends are imposed to replicate the actual bridge conditions. These supports are defined as lines of nodes at the bottom of each girder, modeled by constraining the appropriate degrees of freedom. The left support at the location of the abutment is fixed. The supports at the interior pier, beneath the link slab, are assumed to be pinned. The expansion joint is simulated by a line of roller supports.

### 2.2.2 Material properties

The nonlinear behavior of concrete is simulated using the concrete damage plasticity (CDP) model available in ABAQUS Standard software (ABAQUS, 2020). The CDP is a smeared-cracked model that combines isotropic damage and plasticity concepts for modeling the main two failure mechanisms of concrete: tensile cracking and compressive crushing (ABAQUS, 2020). The input parameters used for the CDP model are summarized in Table 1. The uniaxial tensile behavior of concrete is described through the

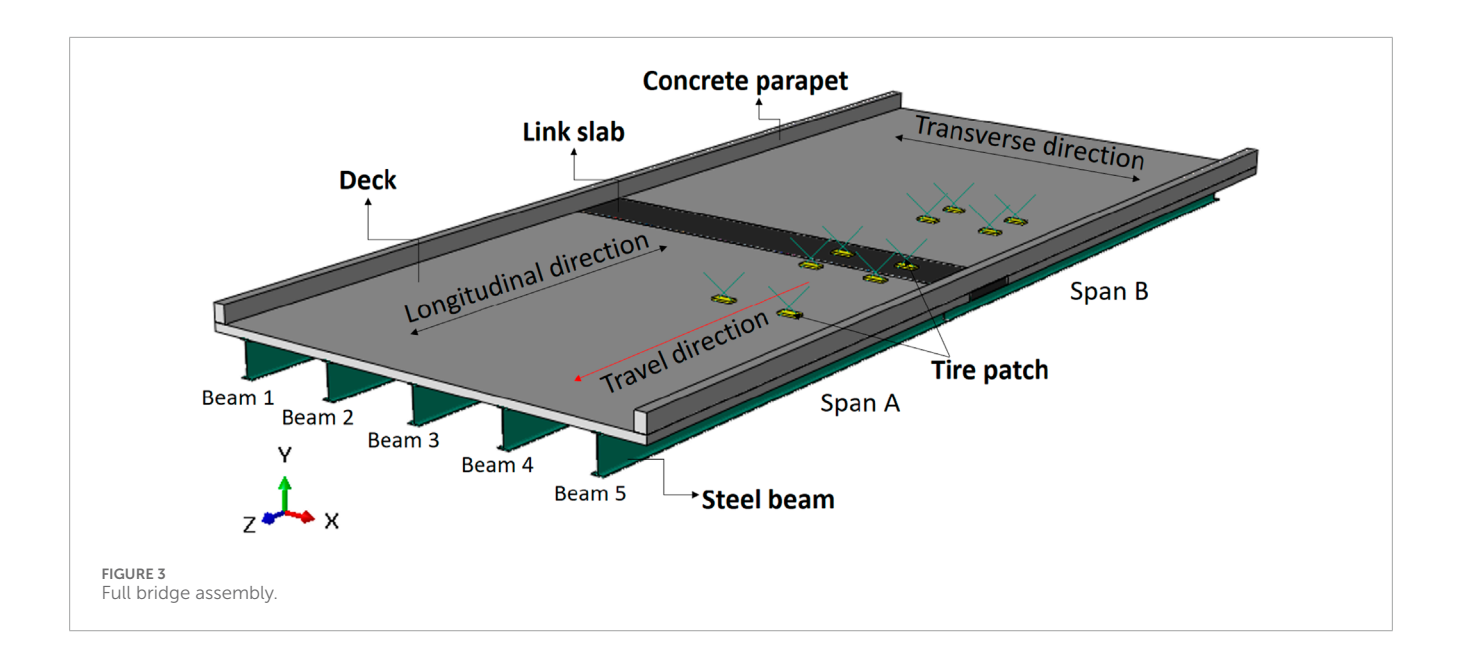


TABLE 1 Input parameters for the CDP model.

Parameters		
Mass density, $\rho$ [kg/m <sup>3</sup> ]	2,300	
Modulus of elasticity, $E_c$ [MPa]	30400	
Poisson's ratio, $v_c$	0.20	
Dilation angle, $\psi$ [deg]	35	
Eccentricity, $\epsilon$	0.10	
Stress ratio, $f_{bo}/f_{co}$	1.16	
Shape factor, $K_c$	0.667	
Viscosity, μ	0.00001-0.001	
Tensile damage, $d_t$	0-0.90	
Compression damage, $d_c$	0-0.80	
Coefficient of thermal expansion, $\alpha$ [m/m/K]	0.000006	
Thermal conductivity, χ [W/m %]	0.80	
Specific heat, $c_p$ [J/kg K]	1,000	

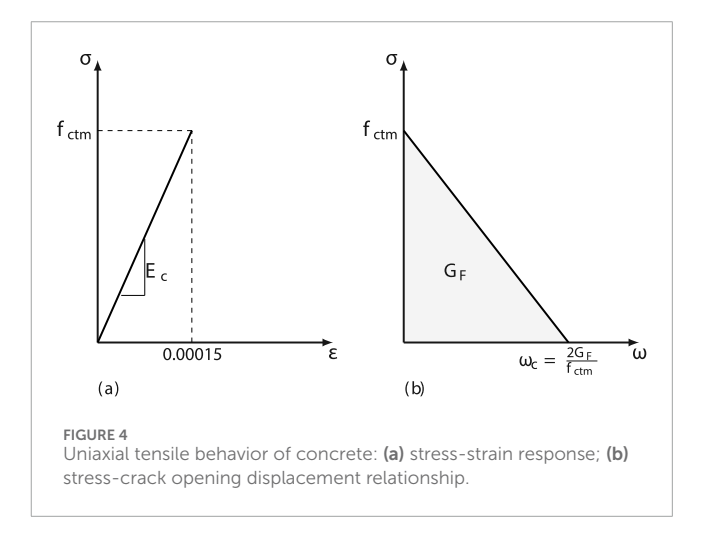
1 MPa, 145 psi.

uniaxial stress-strain and stress-crack opening relationships shown in Figure 4 based on the CEB-FIP Model Code (CEB, 2010).

For the ascending branch, the material response follows the linear stress-strain relationship given in Equation 2 as

$$\sigma_{ct} = E_c \, \varepsilon_{ct} \quad for \quad \sigma_{ct} \le f_{ctm}$$
 (2)

where  $E_c$  is the reduced modulus of elasticity in MPa determined as  $E_c = \alpha_i E_{ci}$ ;  $\alpha_i$  is defined as  $\alpha_i = 0.8 + 0.2 (f_{cm}/88)$ , and cannot be taken greater than 1.0;  $E_{ci}$  is the modulus of elasticity of concrete at the



age of 28 days calculated through  $E_{ci} = E_{co} \alpha_E (f_{cm}/10)^{1/3}$  in which  $E_{co}$  and  $\alpha_E$  are taken as 21500 MPa (3,118 ksi) and 1.0, respectively;  $f_{cm}$  is the mean value of compressive strength estimated as  $f_{cm} = f_{ck} + 8$  MPa;  $f_{ck}$  is the characteristic compressive strength in MPa;  $f_{ctm}$  is the mean value of tensile strength for the concrete in MPa calculated using Equation 3. It is important to note that the stress unit in all the formulations is MPa.

$$f_{ctm} = 0.3(f_{ck})^{2/3} (3)$$

The post-cracking behavior of concrete in tension is represented by a linear softening stress-crack opening displacement relationship  $(\sigma_{ct} - \omega_c)$ . The displacement threshold  $(\omega_c)$  of  $2G_F/f_{ctm}$  is defined in terms of fracture energy  $G_F$  in N/m and the uniaxial tensile strength  $f_{ctm}$ . The fracture energy  $G_F$  represents the energy needed to propagate a unit area of crack surface, calculated in N/m as  $G_F = 73(f_{cm})^{0.18}$ .

The compressive behavior of concrete is defined by the uniaxial stress-strain relationship shown in Figure 5 for unconfined concrete, divided into three parts: 1) An initial uncracked region up to a

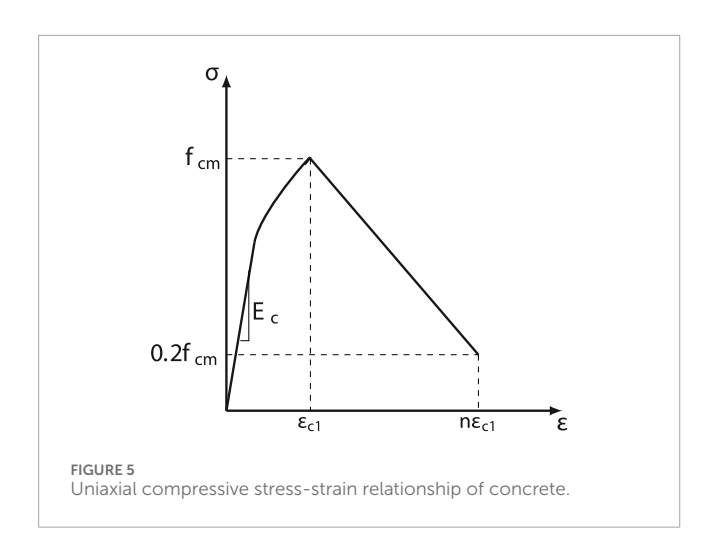


TABLE 2 Coefficient n for defining the cut-off strain CEB (2010).

f <sub>ck</sub> (MPa)	n
20	3.0
40	2.0
60	1.5
80	1.2

1 MPa, 145 psi.

stress of  $0.4f_{cm}$ . 2) The ascending branch between  $0.4f_{cm}$  and  $f_{cm}$ , described by Equations 4–6 as

$$\frac{\sigma_c}{f_{cm}} = -\left(\frac{\kappa \eta - \eta^2}{1 + (\kappa - 2)\eta}\right) for \left|\varepsilon_c\right| < \left|\varepsilon_{c,lim}\right| \tag{4}$$

where

$$\eta = \varepsilon_c / \varepsilon_{c1} \tag{5}$$

$$\kappa = E_c/E_{c1} \tag{6}$$

with  $\sigma_c$  as the compression stress;  $\varepsilon_c$  as the compression strain;  $\varepsilon_{c1}$  as the strain at maximum compressive stress;  $E_{c1}$  as the secant modulus from the origin to the peak compressive stress and  $\kappa$  as the plasticity number (CEB, 2010). 3) The linearly descending portion between the peak and the ultimate compressive stress of  $0.2 f_{cm}$ . The cut-off strain of the descending branch was adjusted with the coefficient n, associated with a compressive strength  $f_{ck}$ , as presented in Table 2.

Stiffness degradation is incorporated into the CDP model by defining the damage parameters for both tension  $(d_t)$  and compression  $(d_c)$ . Concrete damage occurs in the softening branch after the concrete reaches its peak strength. The damage parameters range from 0 to 1, with 0 indicating no damage and one representing complete damage. The specific ranges for  $d_t$  and  $d_c$  used in this study are listed in Table 1. Table 3 provides the material properties for the steel reinforcing bars. The stress-strain curve of the reinforcing bar is assumed to be elastic-perfectly-plastic. The interaction between concrete and steel reinforcement is represented using a perfect bond implemented through an

TABLE 3 Thermal and mechanical properties of steel reinforcement.

Parameters	
Mass density, $\rho_s$ [kg/m <sup>3</sup> ]	7,800
Modulus of elasticity, $E_z$ [MPa]	200000
Poisson's ratio, $v_s$	0.3
Yield strength, $f_{yk}$ [MPa]	440
Ultimate strength, $f_{uk}$ [MPa]	600
Ultimate strain, $\varepsilon_{uk}$ [%]	12
Thermal expansion coefficient, $\alpha$ [m/m/K]	0.0000065
Thermal conductivity, $\chi$ [W/m K]	45
Specific heat, $c_p$ [J/kg K]	480

1 MPa, 145 psi.

embedded constraint. This assumption is commonly adopted in global finite element analyses that focus on capturing overall structural behavior rather than localized bond–slip mechanisms. All thermal and mechanical material properties adopted in this study are based on established design codes (AASHTO, 2017; CEB, 2010) and validated literature sources, ensuring consistency with previous bridge investigations (Caner and Zia, 1998; Wing and Kowalsky, 2005; Aktan et al., 2008; Ulku et al., 2009).

#### 2.2.3 Loading

The bridge structure monitored by Wing and Kowalsky (2005), modeled and analyzed in accordance with the material properties presented in the previous section, is subjected to several loading conditions as described next.

A multiple-step analysis using ABAQUS Standard (ABAQUS, 2020) is conducted to capture the bridge response to applied loads and construction stages accurately. This modeling approach is detailed in Villamizar (2024). The analysis includes three distinct steps. First, the self-weight of the girders and the composite concrete deck is applied under the assumption of simple-span girder behavior. Second, the dead weight of the continuous deck after casting the link slab is incorporated by modifying the interaction properties to represent the continuity provided by the link slab in the negative moment region. This step activates previously deactivated elements at the link slab center and the parapet along the joint gap. The third step applies the live load and temperature gradients through a coupled temperature-displacement analysis (Villamizar, 2024).

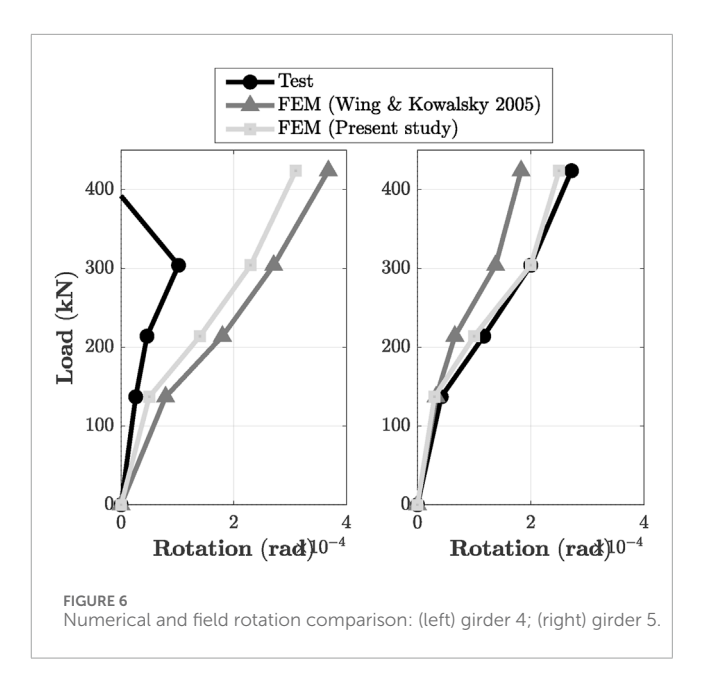
The design live load consists of the vehicular loading HL-93 defined in Section 3.6.1.2 of the AASHTO LRFD Bridge Design Specifications (AASHTO, 2017), combining a design truck or tandem with a lane load. Wheel loads are positioned to maximize force effects on the link slab and are applied using load-controlled options, with tire contact areas modeled via steel plates measuring 0.51 m (20 in.) by 0.25 m (10 in.). Each tire pressure is applied statically and uniformly distributed over the contact area. The spacing between the intermediate and the rear axles is kept at 4.3 m (168 in.) in the present study. The lane load consists of a

9.3 kN/m (0.64 klf) distributed uniformly along the length of the bridge. Transversely, it is assumed to be distributed over a standard design lane of 3 m (120 in.) wide. According to Article 3.6.2 of the specifications (AASHTO, 2017), an impact factor (IM) of 1.33 is applied to the truck or tandem loads but not to the lane load. A surface-to-surface contact interaction between the steel plate and the concrete deck is defined with tangential and normal behaviors. A friction coefficient of 0.6 is specified to define tangential behavior simulating a rough surface. A hard contact pressure-overclosure relationship is used for normal behavior.

The temperature changes are applied following the provisions of Section 3.12 of the AASHTO LRFD Bridge Design Specifications (AASHTO, 2017). The effects of uniform and non-uniform temperature changes are assessed separately. Constant temperature changes are applied in a general static step to all components of the bridge model by creating a predefined temperature field. Both constant changes in temperature, an increase of 25 °C (45 °F) and a decrease of 42 °C (75 °F) are determined using Procedure A defined in Section 3.12.2 of the specifications with the temperatures for a moderate climate for steel bridges. An installation temperature of 24 °C (75 °F) is set as the initial temperature. For the case of nonuniform temperature distributions (Section 3.12.3 (AASHTO, 2017)), the analysis focuses explicitly on solar radiation in Zone 3, considering the actual location of the bridge structure in North Carolina. The design thermal gradients are applied as temperature boundary conditions. It is important to note that the current model is based on a one-way heat flow assumption, that considers temperature variation along the depth of the bridge superstructure only. This model does not account for temperature gradients in the transverse direction of the bridge members (Villamizar, 2024). The influence of these three-dimensional gradients, while relevant, lies beyond the scope of this study.

#### 2.2.4 FE model validation

The analysis described in the previous two sections provided the data to validate the model using test results from Wing and Kowalsky (2005) when subjected to traffic load. The validation process assumes that this loading acts alone and accounts for the prior effect of dead load. The FE model is validated for vehicle loading by placing the truck in the same position as in the live load test to produce the maximum negative moment in the link slab (refer to Figure 3). The results of the present study align with those reported by Wing and Kowalsky (2005). Figure 6 compares the FE and the test rotations at the link slab on Span B along girder lines 4 and 5, respectively. The rotations from the FE model are obtained by dividing the difference in nodal displacement by the vertical distance between the two nodes. The computed rotations at the bridge site are based on the readings from the LVDTs by dividing the displacement difference at each location by the vertical distance between the sensors. Figure 6 includes the results of the FE model developed by Wing and Kowalsky (2005) to verify the field test program for comparison purposes. It is important to emphasize the marked improvement achieved with the numerical model developed in this study compared to the previous grillagebased model by Wing and Kowalsky (2005). This improvement can be attributed to a more accurate geometric representation and the consideration of the CDP material model in this study, which captures the nonlinear behavior of concrete more realistically.

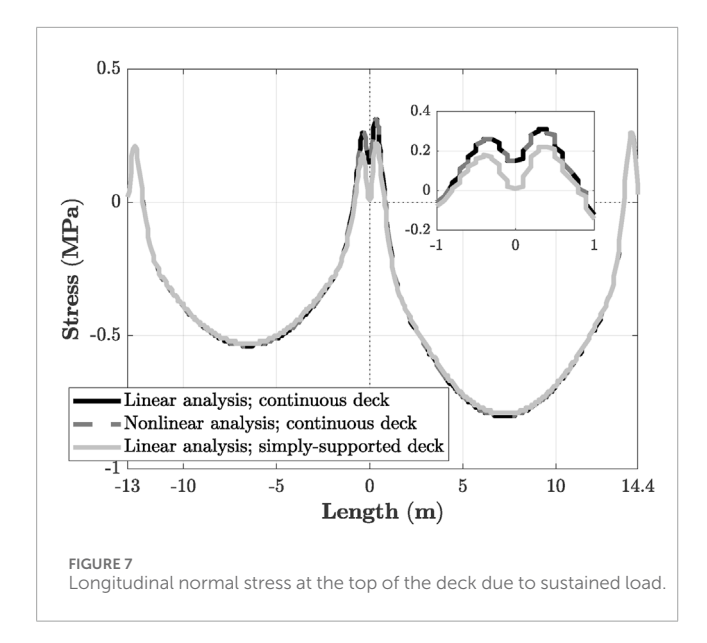


Specifically, for girder 4, discrepancies in sensor readings at this location led to some variation between the test data and the results of the FE model. While the proposed numerical model accurately aligns with the test data in the initial part of the curve, challenges were encountered in validating the model beyond the first point due to sensor-related issues that impacted the experimental data. The scarcity of test data and reported issues with the thermocouples during the monitoring period presented challenges in validating the FE model under temperature gradients. This limitation highlights the need for additional field testing and high-quality monitoring data to enable more robust validation under thermal loading.

# 3 Results

Upon validation of the FE model, as explained in the previous section, the Plott Creek Bridge is subjected to a series of loading conditions to study the effects on the link slabs under various conditions such as (i) dead load, (ii) vehicular traffic loading (HL-93), and (iii) temperature gradients, following the AASHTO LRFD Bridge Design Specifications (AASHTO, 2017). The focus is primarily on the longitudinal tensile stress developed at the top surface of the link slab. This stress parameter is a key metric for identifying potential causes and pinpointing locations where cracking may occur.

Figure 7 depicts the longitudinal normal stress distribution on the top surface of the bridge deck slab when subjected to sustained loads (i.e., self-weight of the steel girders, deck slab, link slab, and concrete parapet). The construction sequence analysis described in 2.2.3 is performed. Both linear elastic and nonlinear analysis results are presented for the jointless bridge deck with a link slab. As can be observed, the tensile stresses developed in the concrete are approximately 0.31 MPa (45 psi) and 0.80 MPa (116 psi) in the negative and positive sections, respectively. These stresses are below the concrete modulus of rupture, indicating that the bridge structure responds elastically under dead loads. No



Linear analysis; continuous deck

Nonlinear analysis; continuous deck

Inear-elastic analysis; simply-supported deck

Linear-elastic analysis; simply-supported deck

Linear-elastic analysis; simply-supported deck

Linear-elastic analysis; simply-supported deck

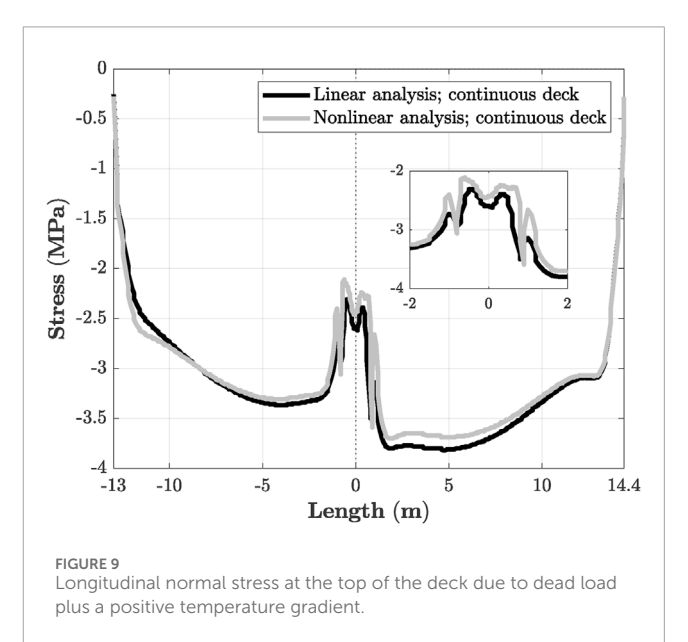
Linear-elastic analysis; sontinuous deck

Longitudinal normal stress at the top of the deck due to dead load plus HL-93 loading.

signs of cracking are noticed at the deck slab due to self-weight. Furthermore, the analysis reveals that the maximum deflection at the center of each simple span (Spans A and B) is approximately 0.0025 m (0.1 in.) and 0.0051 m (0.2 in.), respectively. The calculated girder rotations for Span A and B are approximately 0.00048 rad and 0.00082 rad, respectively. This observed behavior supports the notion that the span bridge behaves close to being simply supported, corroborating the findings of Caner and Zia (1998) regarding the limited contribution of the link slab to the overall flexural stiffness of the bridge structure.

Figure 8 shows the longitudinal normal stresses at the top surface of the concrete deck after applying live loads to the bridge at the critical position in both the longitudinal and transverse directions. The results demonstrate the expected outcome that higher stresses are obtained when either two exterior or interior lanes are simultaneously loaded. The figure presents results from both linear elastic and nonlinear analyses of the jointless bridge deck with a link slab for the purpose of comparison. In the linear analysis, after applying the dead and design live loads on the bridge, the stresses at the top of the link slab can reach up to 4.7 MPa (681 psi). This stress level is twice as high as the concrete tensile strength of 2.2 MPa (321 psi), highlighting the significant influence of truck loading on the occurrence of cracking in the link slabs.

The nonlinear analysis indicates that the maximum stress experienced by the link slab is approximately 1.4 MPa (203 psi), implying that the occurrence of cracking leads to a stress reduction of approximately 70%. This stress reduction highlights the redistribution of forces and stresses in the link slab after cracking. The plastic deformations observed in specific areas on the top surface of the link slab clearly demonstrate its nonlinear behavior. Furthermore, after applying vehicular traffic loading HL-93 to the bridge, the resulting rotation induced at the girder ends is approximately 0.0004 rad on Span A and 0.0022 rad on Span B, respectively. The rotation value of 0.0022 rad on Span B is consistent with the maximum rotation assumed by Wing and Kowalsky (2005) for designing the link slab when considering the girders as simple spans. The highest deflection, near the middle of span B, measures



approximately 0.008 m (0.3 in). Notice in Figure 8 that a simple-span bridge model has also been developed using the same girder dimensions for comparison to the continuous deck slab model.

The longitudinal normal stress distribution on the top surface of the bridge deck slab is investigated when subjected to sustained loads and temperature gradients. The results of the present study show that a uniform temperature change causes an axial force in the link slab of nearly  $534~\rm kN$  ( $120~\rm kips$ ) and bearings displacement along the length of the bridge at the location of the remaining expansion joint of  $0.005~\rm m$  ( $0.2~\rm in$ ). It is observed that temperature differentials cause the link slab to deflect up and down. Figure 9 shows that a positive temperature gradient induces longitudinal compression stresses on the link slab's top surface along the concrete deck's length.

On the other hand, a negative temperature gradient causes tensile stresses on the top surface of the link slab, as illustrated in

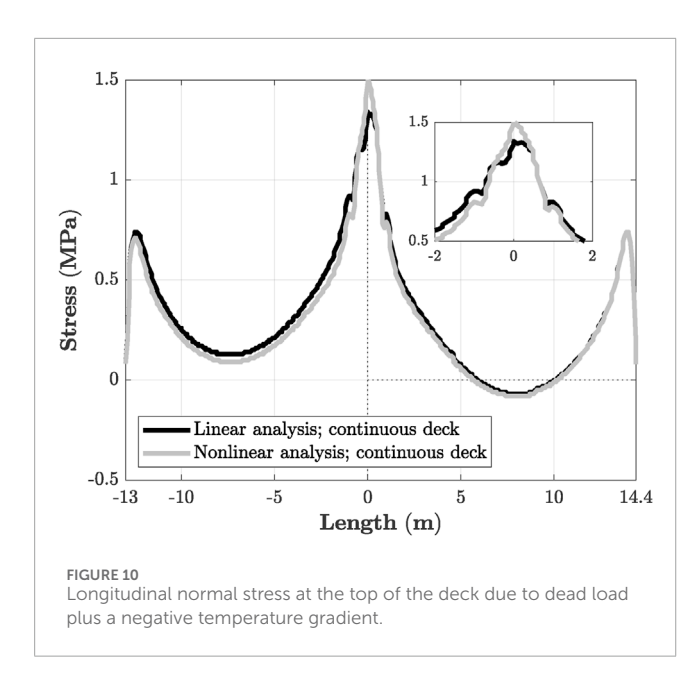


TABLE 4 Girder rotations due to dead load plus vertical temperature gradients.

Loading	Girder rotation [rad]	
	Span A	Span B
Dead load plus a positive temperature gradient	0.00003	0.00101
Dead load plus a negative temperature gradient	0.00033	0.00080

Figure 10. The maximum tensile stress that resulted after imposing the dead load and a negative temperature gradient is near 1.4 MPa (200 psi), which is less than the concrete tensile stress. The estimated girder rotations from ABAQUS, when the bridge is subjected to dead load plus vertical temperature gradients, are presented in Table 4. The rotations are determined between girder ends over interior supports.

The results of the numerical investigation reveal that vehicular traffic loading HL-93 is the primary factor contributing to cracking in the link slabs. However, it is also evident that negative vertical temperature gradients might induce tensile stresses in the link slab. This indicates that temperature gradients should be addressed in the design of link slabs, as they can interact with live loads and lead to critical stress conditions that may result in cracking. Furthermore, the results indicate that as the link slab experiences cracking under service loads, it limits the ability of the connection to transfer load across the joint. These observations aligned with Caner and Zia, (1998) assumption of negligible continuity at the link slab, resulting in the bridge behaving as simply supported rather than a continuous or partially continuous system. As a result, the girder end tends to rotate. A maximum girder rotation of 0.0026 rad is achieved when accounting for the combined effects of live load and temperature gradients in the analyzed bridge structure. This represents a 20% increase in girder rotation compared to when only live load is considered. Cracking occurs mainly at the center part of the link slab, as pointed out during the test program in 1998.

With the successful validation of the FE model, it is now employed to examine the effect of bridge parameters through a parametric study. The predicted response of the bridge is determined in accordance with the criteria outlined in the AASHTO LRFD Bridge Design Specifications (AASHTO, 2017). The results of this comprehensive analysis are presented in the following section.

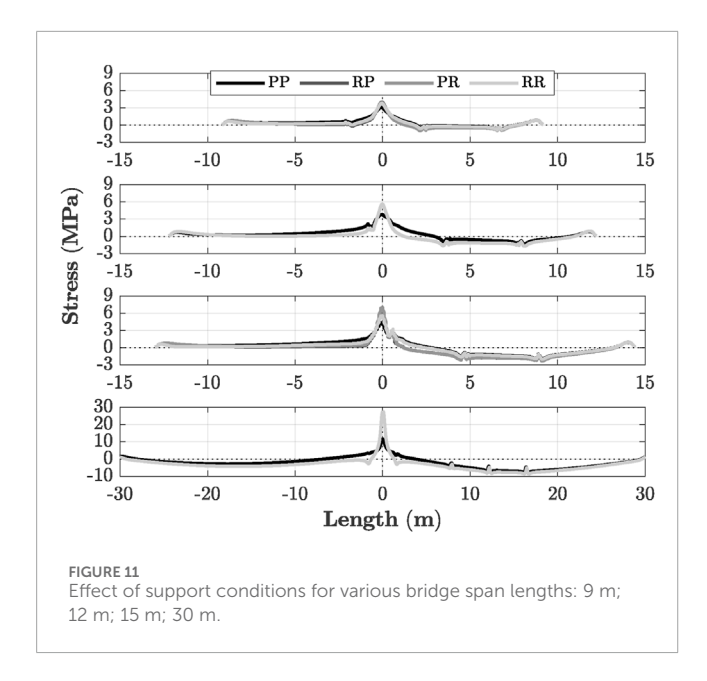
# 4 Parametric study

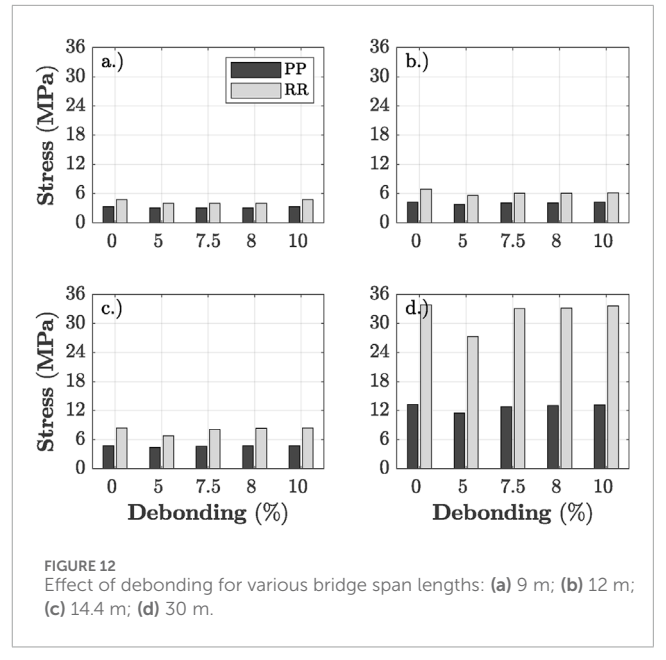
A parametric study is conducted to expand the scope of the analysis by including key variables such as the girder support conditions and the debonded length of the link slab. This study aims to investigate the impact of these variables on the potential for crack initiation in link slabs. The purpose of this work is not to rediscover the influence of multiple factors documented in the literature, but rather to quantify the effects of these two parameters under combined live load and thermal gradients, thereby enabling the practical adaptation of the widely used simplified design framework proposed by Caner and Zia (1998). The selection of bridge design parameters is justified by their well-established significance in previous studies and their continued relevance in current link slab design practices. Each parameter is examined independently to gain a deeper understanding of its impact on the behavior of the link slab. The bridge model is subjected to dead load, vehicular traffic loading HL-93, and the AASHTO negative temperature gradient for Zone 3, with the analysis conducted under linear elastic conditions.

# 4.1 Effect of support conditions

The influence of support conditions is examined by modeling the bridge structure with varied girder restraints at the two intermediate supports (underneath the link slab). Three idealized support conditions are investigated: Pinned-Roller (PR), Roller-Pinned (RP), and Roller-Roller (RR). It is important to note that the first interior support corresponds to the end of the girder at Span A, while the second interior support corresponds to the girder end at Span B. It is worth mentioning that the reference support condition at each girder ends at the intermediate supports aligns with the support conditions used in the bridge studied by Wing and Kowalsky (2005), which is Pinned-Pinned (PP). Since the interest is on examining the influence of the type of supports beneath the link slabs, the boundary condition at the exterior supports remains unchanged during the analysis. It consists of a fixed support at the integral abutment at Span A, which restricts rotation and translation, and a Roller support at the expansion joint on Span B to allow longitudinal movement.

Figure 11 illustrates the stress variations along the bridge length under different support conditions, considering various girder span lengths and a 5% slab debonding. The results indicate that girder support conditions impact the stress distribution within the link slab. Across all support scenarios, the link slab exhibits downward deflection, resulting in tensile stresses at the top surface and compression stresses at the bottom fibers. The stress distribution shown in Figure 11 demonstrates that support arrangements incorporating Roller supports (RR) beneath the link





slabs result in higher longitudinal normal stresses on the link slab compared to those with only Pinned supports (PP). These support conditions represent upper and lower stress bounds, emphasizing the influence of Roller supports on the load transfer mechanism and the consequent increase in stress levels in the link slab. Further analysis reveals that interchanging the position of the Pinned support does not have any significant effect on the response of the link slab. In other words, the stress distribution for support cases RP and PR is nearly identical, suggesting that the specific location of the Pinned support has minimal influence on the behavior of the link slab. For all the boundary conditions considered, the developed stresses in the link slab exceed the concrete tensile strength of 2.2 MPa (321 psi). Additionally, Figure 11 shows the relationship between the span length and the stresses developed at the top fiber of the link slab. As anticipated, the findings suggest a significant increase, approximately fourfold and sevenfold, in longitudinal normal stresses at the top fiber of the link slab when extending the span length from 9 m (30 ft) to 30 m (100 ft) under the PP and RR support conditions, respectively. Moreover, elongating the span length from 15 m (50 ft) to 30 m (100 ft) results in a significant fourfold increase in longitudinal normal stresses at the top fiber of the link slab. An increase of nearly 50% in tensile stresses when RR supports are employed beneath link slabs compared to PP supports. Using PP supports, the tensile stresses can be managed if the span length does not exceed 15 m (50 ft).

# 4.2 Effect of debonded length

In current engineering practice, it is recommended to incorporate a debonded length at the ends of the girders at the joint, extending at least 5% of the girder span length. This debonding length allows the girders to rotate under the bridge actions. It also helps to transfer the strains and stresses between the deck slab and the girders. A debonding length of 5% of the span was suggested by prior research (ElSafty, 1994; ElSafty and Okeil, 2008)

with the argument that it does not significantly alter the deflection characteristics of the link slab. In this parametric study, the size of the debonded zone is increased from 5% to 10% of the span length to investigate the effect on the developed stresses at the link slabs. A configuration with a bonded link slab (where no debonding is present, i.e., 0% of the span length debonded) is included for reference.

The results in Figure 12 demonstrate that using a debonded length of 5% reduces normal longitudinal stresses at the top surface of the link slab by approximately 7% if compared against a bonded link slab with only Pinned and Roller supports, respectively. The reduced normal longitudinal stresses with an increased debonded zone size can be attributed to the increased rotational freedom allowed at the joint. By providing a larger debonded zone, the link slab experiences less restraint, allowing for better load redistribution and reduced stress concentrations. These findings agree with those reported in (Aktan et al., 2008; ElSafty and Okeil, 2008). However, the results also indicate that the debonded length in the link slab should not exceed 7.5% of the span. Beyond this point, the debonding becomes less effective as the ends of the link slab tend to rotate more, leading to higher tensile stresses at the top surface of the link slab. The decrease in stresses within the link slab when maintaining debonding within the range of 5%-7.5% of the span length can be also explained by the adjustment in the link slab length within the limits of the inflection points for the negative moment region. As the debonded length increases beyond this range, the link slab becomes longer, extending into the positive moment region, leading to higher stresses.

# 5 Conclusion

This paper presents a computational model developed in ABAQUS software (ABAQUS, 2020) based on the Plott Creek Bridge in Haywood country, North Carolina, originally investigated by Wing and Kowalsky (2005). The model provides a detailed

simulation of the behavior of a rehabilitated steel-concrete bridge structure that incorporates link slabs. It is validated through comparisons with experimental data and subjected to traffic loads and temperature gradients according to the provisions of the AASHTO LRFD Bridge Design Specifications (AASHTO, 2017). A parametric study is conducted to assess the influence of support conditions at the interior pier ends of the girders and slab debonded length on the potential for crack initiation in link slabs. The numerical analyses indicate the substantial impact of traffic load and vertical temperature gradients on inducing stresses in the link slabs, ultimately resulting in observed cracks in the field.

The current design practice for debonded link slabs follows the simplified framework proposed by Caner and Zia (1998). This method models the link slab as a pure bending element that resists moments generated by girder end rotations under live load plus impact, assuming simple-span girders and neglecting continuity across the joint. In this paper, the range of considerations in design is extended to include the type of girder support, length of link slab debonding, and temperature effects. The novelty of this study lies in quantifying the influence of these parameters within the widely adopted simplified framework, thereby providing practical guidance for enhancing its applicability and accuracy in engineering practice. The findings described in this paper confirm the simply supported condition for the link slab analysis. However, vertical temperature gradient effects across the section should also be accounted for in the design of link slabs. It is found that tensile stresses caused by a negative temperature gradient in combination with those resulting from the live load may contribute to developing cracks in the link slabs. Specifically, the combination of live load and a negative temperature gradient is identified as the most critical loading that influences the occurrence of cracking in the link slab. The results of this study indicate that temperature gradients increase the girder end rotation obtained from live load analysis for simply supported beams by 20% in the range of parameters considered in the parametric study. From these results, the following conclusions can be drawn:

- 1. The girder support conditions impact the stress distribution in the link slabs. The highest stresses are observed when roller supports are employed beneath the link slab, encompassing Roller-Roller, Roller-Pinned, and Pinned-Roller support configurations. Specifically, using roller supports beneath link slabs can increase tensile stresses by approximately 50% compared to pinned supports. However, the use of pinned supports can be effective if the span length is less than 15 m (50 ft) Thus, it is recommended to use elastomeric bearings to accommodate horizontal movements resulting from girder translation and rotation. Elastomeric bearings provide flexibility and can effectively absorb these movements, reducing stress concentrations and improving the overall performance of the link slab connection.
- 2. The use of debonded link slabs has a minor effect on the overall behavior of the bridge. Nevertheless, it does influence the local stress distribution within the link slab region. It is recommended to include debonding in the link slab design and to keep it within the range of 5%-7.5% of the span length to reduce stress concentrations and enhance the overall performance of the link slab. This practice results in a reduction of normal longitudinal stresses at the top surface of

the link slab by approximately 7% when compared to a fully bonded link slab configuration.

The authors acknowledge that the findings of this study are based on the specific geometry and site conditions of the Plott Creek Bridge. Thermal stresses and rotations are inherently context-dependent and influenced by factors such as climate, material properties, and girder stiffness; therefore, these variables should be carefully considered when applying the present results to other bridge configurations.

# Data availability statement

The original contributions presented in the study are included in the article/supplementary material, further inquiries can be directed to the corresponding authors.

### **Author contributions**

SV: Formal Analysis, Writing – original draft. OA: Validation, Writing – review and editing. DG: Validation, Writing – review and editing. JR: Methodology, Supervision, Validation, Writing – review and editing. GH: Methodology, Supervision, Validation, Writing – review and editing.

# **Funding**

The author(s) declare that financial support was received for the research and/or publication of this article. The authors gratefully acknowledge the financial support provided by the Joint Transportation Research Program at Purdue University, in collaboration with the Indiana Department of Transportation and the Federal Highway Administration, through research project FHWA/JTRP-SPR 4223. The authors also sincerely appreciate the support provided by Colfuturo and Colciencias, Colombia. This research has been funded by Dirección General de Investigaciones of Universidad Santiago de Cali under call No. DGI-01-2025.

# Conflict of interest

The authors declare that the research was conducted in the absence of any commercial or financial relationships that could be construed as a potential conflict of interest.

# Generative AI statement

The author(s) declare that no Generative AI was used in the creation of this manuscript.

Any alternative text (alt text) provided alongside figures in this article has been generated by Frontiers with the support of artificial intelligence and reasonable efforts have been made to ensure accuracy, including review by the authors wherever possible. If you identify any issues, please contact us.

#### Publisher's note

All claims expressed in this article are solely those of the authors and do not necessarily represent those of their affiliated organizations, or those of the publisher, the editors and the reviewers. Any product that may be evaluated in this article, or claim that may be made by its manufacturer, is not guaranteed or endorsed by the publisher.

# References

AASHTO (2017). "Bridge design specifications and commentary," in *Aashto LRFD* (Washington, DC: American Association of State Highway and Transportation Officials)

ABAQUS (2020). Analysis user's manual 6.10EF. Providence, RI: Dassault Systems Simulia Corp.

Aktan, H., Attanayake, U., and Ulku, E. (2008). Combining link slab, deck sliding over backwall, and revising bearings. Report. No. RC-1514. Kalamazoo, MI: Michigan Department of Transportation.

Au, A., Lam, C., Au, J., and Tharmabala, B. (2013). Eliminating deck joints using debonded link slabs: research and field tests in Ontario. *J. Bridge Eng.* 18, 768–778. doi:10.1061/(ASCE)BE.1943-5592.0000417

Caner, A. (1996). *Jointless bridge decks supported by simple span girders. Ph.D. thesis.* Raleigh, NC: North Carolina State University.

Caner, A., and Zia, P. (1998). Behavior and design of link slabs for jointless bridge decks. PCI J. 43, 68–80. doi:10.15554/pcij.05011998.68.80

Caner, A., Dogan, E., and Zia, P. (2002). Seismic performance of multisimple-span bridges retrofitted with link slabs. *J. Bridge Eng.* 7, 85–93. doi:10.1061/(asce)1084-0702(2002)7:2(85)

CEB (2010). CEB-FIP model code 2010: design code. Thomas Telford.

Culmo, M. P., Marsh, L., and Stanton, J. (2017). Recommended AASHTO guide specifications for ABC design and construction. Washington, D.C: Transportation Research Board. Final Report for Project 12-102, National Cooperative Highway Research Program.

ElSafty, A. (1994). Behavior of jointless bridge decks. Raleigh, NC: North Carolina State University. Ph.D. thesis.

ElSafty, A., and Okeil, A. (2008). Extending the service life of bridges using continuous decks. *PCI J.* 53, 96–111. doi:10.1061/(ASCE)1084-0680(2005)10:4(229)

Fu, C. C., and Zhu, Y. F. (2017). "A pilot application of link slab with selected material for MDTA steel bridges,". Baltimore, MD. *Tech. Rep. Md. Transp. Auth.* 

Garber, D., McDonagh, M., Sakellos, G., Chong, C., Ocel, J. M., Graybeal, B. A., et al. (2023). *UHPC link slab design example*. United States: Tech. rep.

Gastal, F. (1986). Instantaneous and time-dependent response and strength of jointless bridge beams. Raleigh, NC: North Carolina State University. Ph.D. thesis.

Gastal and Zia (1989). "Analysis of bridge beams with jointless decks," in International association for bridge and structural engineering (IABSE), 555–560.

Gergess, A. N. (2019). Analysis of bonded link slabs in precast, prestressed concrete girder bridges.  $PCIJ.\ 64.\ doi:10.15554/pcij64.3-03$ 

Gergess, A. N., and Hawi, P. F. (2019). Structural behavior of debonded link-slabs in continuous bridge decks. *J. Bridge Eng.* 24, 04019030. doi:10.1061/(asce)be.1943-5592.0001388

Haikal, G., Ramirez, J., Jahanshahi, M., Villamizar, S., and Abdelaleim, O. (2019). "Link-slabs details and material," West Lafayette. *Final Rep. No. FHWA-IN-JTRP-2019-10, Jt. Transp. Res. Program.* doi:10.5703/1288284316920

Hong, Y. (2014). Analysis and design of link slabs in jointless bridges with fibre-reinforced concrete. Waterloo, Ontario, Canada: University of Waterloo. Master's thesis.

Hou, M., Hu, K., Yu, J., Dong, S., and Xu, S. (2018). Experimental study on ultrahigh ductility cementitious composites applied to link slabs for jointless bridge decks. *Compos. Struct.* 204, 167–177. doi:10.1016/j.compstruct.2018.07.067

Jirawattanasomkul, T., Kongwang, N., Likitlersuang, S., Yodsudjai, W., Charuvisit, S., and Sato, Y. (2021). Failure analysis of dapped-end cracking in posttensioned bridge girder. *J. Bridge Eng.* 26, 04021082. doi:10.1061/(asce)be.1943-5592.0001786

Karim, R., and Shafei, B. (2021). Performance of fiber-reinforced concrete link slabs with embedded steel and GFRP rebars. *Eng. Struct.* 229, 111590. doi:10.1016/j.engstruct.2020.111590

Kim, Y., Fischer, G., and Li, V. C. (2004). Performance of bridge deck link slabs designed with ductile engineered cementitious composite. *ACI Struct. J.* 101, 792–801. doi:10.14359/13454

Larusson, L., Reyes, J., Lum, B., Fischer, G., and Robertson, I. N. (2013). "Development of flexible link slabs using ductile fiber reinforced concrete,". Honolulu, HI: No. UHM-CEE-13-04, Hawaii Department of Transportation. *Final Rep.* 

Leiva-maldonado, S., Bowman, M. D., and Gomez, D. (2023). Life-cycle cost profiles selection for different superstructure bridge types. *Structures* 54, 1–13. doi:10.1016/j.istruc.2023.04.105

Lepech, M. D., and Li, V. C. (2008). Large-scale processing of engineered cementitious composites. ACI Mater. J. 105, 358–366. doi:10.14359/19897

Lepech, M. D., and Li, V. C. (2009). Application of ECC for bridge deck link slabs. *Mater. Struct.* 2009, 1185–1195. doi:10.1617/s11527-009-9544-5

Li, V., Fischer, G., Kim, Y., Lepech, M., Qian, S., Weimann, M., et al. (2003). *Durable link slabs for jointless bridge decks based on strain-hardening cementitious composites. Report. No. RC-1438.* Lansing, MI: Michigan Department of Transportation.

Li, V., Lepech, M., and Li, M. (2005). Field demonstration of durable link slabs for jointless bridge decks based on strain-hardening cementitious composites. Report. No. RC-1471. Lansing, MI: Michigan Department of Transportation.

Li, V., Yang, E., and Li, M. (2008). Field demonstration of durable link slabs for jointless bridge decks based on strain-hardening cementitious composites-phase 3: shrinkage control. Report. No. RC-1506. Lansing, MI: Michigan Department of Transportation.

Luo, Y., Yan, Q., Yue, X., Jia, B., Yu, X., and Chen, Y. (2024). A new analytical method for link slab analysis. KSCE J. Civ. Eng. 28, 800–816. doi:10.1007/s12205-024-0826-9

Ozyildirim, H. C., Khakimova, E., Nair, H., and Moruza, G. M. (2017). Fiber-reinforced concrete in closure pours over piers. *ACI Mater. J.* 114, 397–406. doi:10.14359/51689561

Qian, S., Lepech, M. D., Kim, Y. Y., and Li, V. C. (2009). Introduction of transition zone design for bridge deck link slabs using ductile concrete. *ACI Struct. J.* 106, 96–105. doi:10.14359/56288

Reyes, J., and Robertson, I. N. (2011). "Precast link slab for jointless bridges decks,". Honolulu, HI: No. UHM-CEE-11-09, Hawaii Department of Transportation. *Final Rep.* 

Saber, A., and Aleti, A. R. (2012). Behavior of FRP link slabs in jointless bridge decks. Adv. Civ. Eng. 2012, 1-9. doi:10.1155/2012/452987

Shafei, B., Taylor, P. C., Phares, B. M., Najimi, M., Karim, R., Hajilar, S., et al. (2018). Material design and structural configuration of link slabs for ABC applications.

Srivaranun, S., Tannawee, T., Jirawattanasomkul, T., Jongvivatsakul, P., Sato, Y., and Likitlersuang, S. (2024). Field investigation and numerical analysis of horizontal cracking in ledge girders of post-tension concrete bridges. *Eng. Struct.* 307, 117866. doi:10.1016/j.engstruct.2024.117866

Ulku, E., Attanayake, U., and Aktan, H. (2009). Jointless bridge deck with link slabs design for durability. *Transp. Res. Rec. J. Transp. Res. Board Journal Transp. Res. Board* 1, 68–78. doi:10.3141/2131-07

Villamizar, S. (2024). Effect of temperature gradients and girder support conditions on the behavior of bridge deck link slabs. West Lafayette, IN: Purdue University. Ph.D. thesis

Wang, Z., Gao, H., Wang, H., and Chen, Z. (2019). Development of stiffness-adjustable tuned mass dampers for frequency retuning. *Adv. Struct. Eng.* 22, 473–485. doi:10.1177/1369433218791356

Wing, K. M., and Kowalsky, M. J. (2005). Behavior, analysis, and design of an instrumented link slab bridge. *J. Bridge Eng.* 10, 331–344. doi:10.1061/(ASCE)1084-0702(2005)10:3(331)

Zhang, J., Li, V. C., Nowak, A. S., and Wang, S. (2002). Introducing ductile strip for durability enhancement of concrete slabs. *J. Mater. Civ. Eng.* 14, 253–261. doi:10.1061/(asce)0899-1561(2002)14:3(253)

Zheng, Y., Zhang, L., and Xia, L. (2018). Investigation of the behaviour of flexible and ductile ECC link slab reinforced with FRP. Constr. Build. Mater. 166, 694–711. doi:10.1016/j.conbuildmat.2018.01.188

Zhong, J., Shen, J., Wang, W., Shi, J., Yang, X., and Zhou, G. (2019). Working state of ECC link slabs used in continuous bridge decks. *Appl. Sci.* 9, 4667. doi:10.3390/app9214667